International Journal of Nanomedicine

Dovepress
Taylor & Francis Group

ORIGINAL RESEARCH

Dual-Spherical Multifunctional Nanomotors for Intravesical Bladder Cancer Therapy

Yiyang Chen[1,2,*], Bin Zheng[1,*], Zhenghong Liu[1,*], Heng Wang[1], Lihui Xu[3], Xiaowen Qin[1], Li Sun[1], Haichang Li[1], Wentao Xu[1], Yixuan Mou[1], Chenkai Wang[1], Xintao Hua[1], Xuanyi Zhou[1], Dingyi Liu[1], Wenyan Zuo[1], Chunnan Zhang[1], Pu Zhang[1], Dahong Zhang[1,2]

[1]Urology & Nephrology Center, Department of Urology, Zhejiang Provincial People's Hospital (Affiliated People's Hospital), Hangzhou Medical College, Hangzhou, Zhejiang, People's Republic of China; [2]The Second School of Clinical Medicine, Zhejiang Chinese Medical University, Hangzhou, Zhejiang, People's Republic of China; [3]School of Pharmacy, Hangzhou Normal University, Hangzhou, Zhejiang, People's Republic of China

*These authors contributed equally to this work

Correspondence: Pu Zhang; Dahong Zhang, Email zhangpuxjtuer@163.com; zhangdahong666@163.com

Background: Conventional intravesical chemotherapy for bladder cancer has shown limited clinical efficacy. To overcome this challenge, self-propelled nanomotors, including urease-modified nanomotors, have been developed. These nanomotors enhance drug diffusion in urine, offering advantages over traditional drugs and passive nanoparticles. However, a key issue remains: the inability to maintain long-term urease activity.

Methods: Nanozymes, glucose oxidase, and urease are synthesized into a three-enzyme nanomotors via biomineralization, serving as a power source. Cell membrane nanoparticles loaded with gemcitabine were combined with three-enzyme nanomotors to form dual-spherical nanomotors. TEM, DLS, and analyses of urease/glucose oxidase activity and nanomotor trajectories confirmed successful nanomotor fabrication. These nanomotors can regulate tumor cell glucose metabolism and release gemcitabine upon cellular entry, achieving a dual anticancer effect.

Results: Nanomotors synthesized through biomineralization methods exhibit the ability to retain long-term activity. After intravesical instillation, urease-containing nanomotors decomposed urea to produce carbon dioxide and ammonia, propelling rapid nanoparticle movement for deep bladder wall penetration. The homing ability of the tumor membrane-coated nanoparticles enhanced nanomotor accumulation in tumor cells. Subsequently, the nanomotors release Gox and gemcitabine, which significantly inhibit tumor progression.

Conclusion: This innovative strategy utilizes gemcitabine - loaded nanomotors to penetrate the mucus layer and target tumors, inducing cell death for the treatment of bladder cancer.

Keywords: bladder cancer, nanomotor, intravesical therapy

Introduction

Bladder cancer (BCa), a prevalent malignant tumor in the urinary system,[1] poses significant health challenges. For non-muscle-invasive bladder cancer and cases with high risks of recurrence and progression, postoperative intravesical instillation is a critical adjuvant therapy. It improves treatment outcomes and inhibits tumor growth by directly instilling drugs via a catheter into the bladder, allowing them to contact the mucosal surface and reducing systemic toxicity.[2–4] However, the effectiveness of this approach is often compromised by short drug retention times, poor drug penetration, and rapid clearance due to periodic urination.[5] These factors lead to suboptimal therapeutic effects, potentially causing cancer recurrence or progression and necessitating radical cystectomy, a surgery with considerable impacts on patients' quality of life and prognosis.[6]

Against this backdrop, self - powered nanoparticles (nanomotors), have come to the fore as drug delivery systems.[7–10] Their superior mobility allows them to navigate complex fluid environments,[11,12] which is typically beyond the reach of

Received: 19 July 2025
Accepted: 21 November 2025
Published: 6 December 2025

drugs and passive nanoparticles. By transforming the chemical energy of the surrounding fluid into mechanical thrust, nanomotors pave the way for biomedical applications.

Glucose oxidase (Gox) catalyzes the conversion of glucose to gluconic acid and hydrogen peroxide (H_2O_2),[13] offering a strategy to modulate tumor glycolysis.[8,14] However, this reaction consumes oxygen (O_2), and the hypoxic conditions often found in tumors can inhibit it.[15] Chen et al[16] developed a bio-mineralization strategy to create Gox-Mn nanoparticles combining nanozyme and Gox activities. Manganese-containing nanozymes generate O_2 from H_2O_2 in the tumor microenvironment,[17] supporting Gox's glucose consumption and glycolysis.[18] The generated H_2O_2 further enhances nanozyme activity.[19] This system merges two catalytic reactions into a self-amplifying cycle, intensifying glucose depletion and promoting cancer starvation therapy.

Using this strategy, we developed a novel multifunctional nanomotor (UG-M@Gem) by conjugating Gem - loaded tumor - membrane nanoparticles (M@Gem) with triple - enzyme - active nanoparticles (UG, composed of manganese ions, Gox, and urease). This design leverages the catalytic activities of the enzymes to enhance drug delivery and efficacy. In contrast to the complex synthesis steps required for traditional nanomotors[1,2] and the challenge of rapid inactivation of urease, this study simply conjugates drug - loaded membrane nanoparticles with the power source (UG) to achieve asymmetric distribution of urease. Moreover, the biomineralization synthesis method can significantly maintain the activity of urease (Figure S1A). Following intravesical instillation, the urease asymmetrically distributed on the nanomotors catalyzes the conversion of urea in urine into carbon dioxide and ammonia. This reaction generates a self - propulsion force for rapid nanoparticle movement, enabling deep penetration into the bladder wall. The tumor - membrane homing directs the nanomotors to gather at tumor sites, achieving targeted and deep - penetrating tumor treatment. As shown in Figure 1, once tumor cells internalize UG - M@Gem, Gox oxidizes intratumoral glucose to produce gluconic acid and H_2O_2, creating an H_2O_2 - rich microenvironment. The released manganese ions then catalyze H_2O_2 into O_2, offsetting Gox's O_2 consumption. This self - amplified glucose depletion effectively kills tumor cells. Meanwhile, Gem in the membrane nanoparticles is gradually released. Notably, all nanomotor components are biocompatible, showing potential for clinical translation.

Materials and Methods

Manganese chloride tetrahydrate (MnCl2.4H2O) was purchased from Sigma (China). Urease, Gemcitabine (Gem), glucose oxidase, Chlorpromazine (CPZ), filipin, aminoyl isopropyl ethyl ester (EIPA) were purchased from MedChemExpress (China). NHS-PEG-DBCO was purchased from Tanshtech (China). Azide-choline was purchased from Xi'an ruixi Biological Technology Co.,Ltd (China). Ethyl acetate, poly(lactic-co-glycolic acid) (PLGA) (Mw 38000–54000) was obtained from Macklin BiochemicalCo., Ltd. (China), Endoplasmic reticulum (ER) tracker, Golgi apparatus (GA) tracker, Lysosomes (Lyso) tracker and the Cell Counting Kit-8 (CCK-8) was obtained from Yeasen Biotech Co., Ltd. (China). Potassium fluorescein was obtained from LABLEAD. Inc. (China).

Cell Membrane Derivation

T24 cells (1×10^6) were incubated with 200 μM Azide-choline for 24 hours. The cells were then washed three times with PBS, scraped, and resuspended in hypotonic buffer to produce cell membrane fragments. The resulting mixture was centrifuged at 700×g for 10 minutes at 4°C, followed by centrifugation at 14,000×g for 30 minutes at 4°C to obtain purified cell membrane fragments.

Synthesis and Characterization of Cell Membrane-Coated Nanoparticles

M@Gem nanoparticles were prepared using a solvent evaporation method. PLGA (10 mg) and gemcitabine (Gem, 1 mg) were dissolved in ethyl acetate. The solution was added to ultrapure water under vigorous stirring. After the volatile organic solvent evaporated, 1 mL of the suspension was mixed with cell membrane fragments (0.3 mg) and transferred to a mini - extruder (Avanti Polar Lipids) with a polycarbonate membrane (400 nm pores). After repeated extrusion, the product was centrifuged at high speed, rinsed with sterile ultrapure water, and dried to obtain membrane - coated nanoparticles (M@Gem). The particle size and zeta potential of M@Gem were measured using dynamic light scattering (DLS, Litesizer™500, AntonPaar, Graz, Austria).

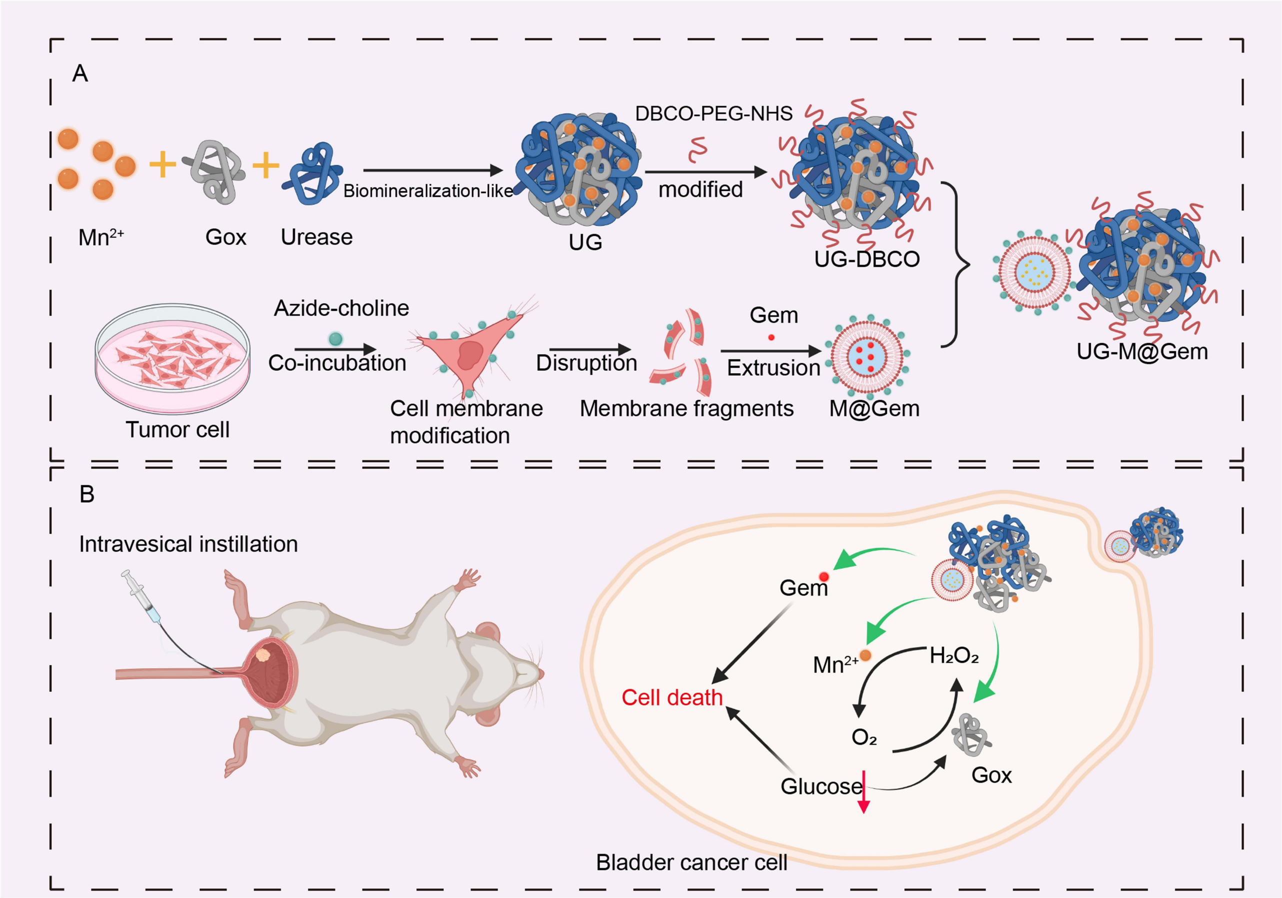

Figure 1 A multifunctional dual-spherical nanomotor for intravesical therapy of BCa. (**A**) The preparation process of dual-spherical nanomotors. The text below the black arrow in the picture indicates the processing method of nanomotor. (**B**) The process of intravesical therapy in vivo (Left) and anti-tumor cells through starvation therapy and chemotherapy (Right). The green arrow in the figure indicates the release of the nanomotor component. The synergistic action of the two enzymes leads to a self-amplifying consumption of glucose (indicated by the red arrow representing the decrease in glucose levels), which, together with Gem, results in cell death.

Synthesis and Characterization of UG

UG nanoparticles were prepared by mixing Gox (1.5 mg/mL, 500 µL), urease (1.5 mg/mL, 500 µL), and 2 - methylimidazole (IMI; 7.5 mg/mL, 500 µL) and incubating for 30 minutes. $MnCl_2$ (3 mg/mL, 500 µL) was then added to the mixture. After 1 hour, the solution was centrifuged at 12,000 rpm for 20 minutes to obtain UG. The particle size and zeta potential of UG were characterized by dynamic light scattering (DLS).

Synthesis and Characterization of UG-M@Gem

To prepare UG-M@Gem, equal volumes of UG and M@Gem were first analyzed using Nano-particle Tracking Analysis (NTA) to determine the number of nanoparticles. UG was then mixed with NHS-PEG-DBCO (M.W. 1000) at a molar ratio of 1:10000 and incubated for 30 minutes. The mixture was centrifuged at 12,000 rpm for 20 minutes to obtain UG-DBCO. Subsequently, equimolar amounts of M@Gem and UG-DBCO were mixed and incubated for 1 hour to form UG-M@Gem. The particle size and zeta potential of UG-M@Gem were measured using DLS.

Nanomotor Migration Assay

The movement of UG-M@Gem was observed using a fluorescence inverted microscope. 50 µL of UG-M@Gem solution was added to 950 µL of urea solution at varying concentrations (0, 100, 300, and 500 mM). The motion of nanoparticles was recorded at 25 frames per second for 20 seconds. Python-based software was used to analyze the motion trajectories of UG-M@Gem from the recorded videos.[20] The mean squared displacement (MSD) was calculated using the formula

$MSD(\Delta t) = [(x_i(t + \Delta t) - x_i(t))^2]$ (i = 2 for two-dimensional analysis). The diffusion coefficient (D) was determined using the equation $MSD(\Delta t) = 4D\Delta t$, applicable for small particles with low rotational diffusion at short time intervals. Over 30 particles were analyzed per group to obtain statistical data.

In vitro Release of Gemcitabine

The release efficiency of Gem from different formulations was evaluated in PBS (pH 7.4) or urine at 37°C. M@Gem or UG-M@Gem (2 mL) was placed in a dialysis bag (molecular weight cutoff: 3.5 kDa), which was then immersed in PBS or urine and shaken at 70 rpm/min at 37°C. At predetermined intervals, 1 mL of the dialysate was transferred for HPLC analysis. Each data point resulted from three tests across three independent experiments.

Catalytic Ability of Nanoparticles on Glucose Depletion

UG-M@Gem (10 mg/mL) was incubated with various glucose concentrations (0–1000 mg/mL) at room temperature for 48 hours. Following incubation, the solution was collected and analyzed for hydrogen peroxide using a detection assay kit and for pH changes using a pH meter.

Mucus-Penetration Assay

The mucus layer was gently scraped and collected in a centrifuge tube. Centrifugation was performed at 1000 g for 30 minutes, repeated twice, and the supernatant was collected and filtered through a Transwell insert with a 0.4 μm pore size polyester membrane. UG-M@Gem were incubated with Dil (10 μM) for 30 minutes, followed by centrifugation at 12,000 rpm to remove free Dil. Urea solutions at different concentrations (100, 300, 500 mM, 90 μL) were mixed with UG-M@Gem (10 mg/mL, 10 μL) and added to the upper chamber of the Transwell insert, with 1 mL of PBS in the lower chamber. After 2 hours, the PBS from the lower chamber was collected and analyzed for drug concentration by HPLC or for fluorescence using a multimode microplate reader.

Cell Culture

BCa cells (T24 and 5637) were cultured in RPMI 1640 medium, and normal urothelial cells (SVHUC-1) were cultured in F12K medium. All cells were maintained in a humidified incubator at 37°C with 5% CO_2. The culture medium was refreshed every 2 days. When cells reached 80–90% confluence, they were trypsinized for passaging. All cell were obtained from the National Collection of Authenticated Cell Cultures, China.

BCa Targeting Efficiency

SVHUC-1, T24, and 5637 cells were seeded in confocal culture dishes at 5×10^4 cells per well. During the synthesis of UG-M@Gem, coumarin-6 (2 mg/mL) was used in place of gemcitabine. After 12 hours of incubation in a medium containing 300 mM urea, cells were treated with UG-M@Gem (with Coumarin-6 substituting for Gem) for 2 hours. Following three PBS washes, cells were examined using confocal laser scanning microscopy (CLSM) to assess BCa targeting efficiency, with ImageJ software used for analysis. For flow cytometry, cells were processed similarly, transferred to a flow cytometer (BD Biosciences, New Jersey, US), and analyzed by counting 1×10^4 cells to determine mean fluorescence intensity. Experiments were repeated three times independently, and data were analyzed using FlowJo software.

Endocytosis Pathway Determination

T24 and 5637 cells were seeded in confocal culture dishes at 5×10^4 cells per well and incubated for 12 hours. To inhibit specific endocytic pathways, cells were treated with endocytosis inhibitors: filipin (1 μg/mL), CPZ (10 μg/mL), or EIPA (10 μg/mL) for 1 hour. Incubation at 4°C was used to block energy-dependent endocytosis. UG-M@Gem were incubated with Dil (10 μM) for 30 minutes, followed by centrifugation at 12,000 rpm to remove free Dil. Fluorescently labeled UG-M@Gem (0.3 mg/mL, 100 μL) was then incubated with pre-treated cells or with cells in a medium containing 300 mM urea at 4°C for 2 hours. Cells were washed three times with PBS and stained with Hoechst for nuclear visualization. Fluorescence was observed via CLSM, and images were analyzed using ImageJ software.

Intracellular Colocalization of UG-M@Gem

T24 and 5637 cells were seeded in confocal culture dishes at a density of 5×10^4 cells per well and incubated for 12 hours. UG-M@Gem were incubated with Dil (10 μM) for 30 minutes, followed by centrifugation at 12,000 rpm to remove free Dil. Fluorescently labeled UG-M@Gem (0.3 mg/mL, 100 μL) was then incubated with T24 and 5637 cells in a medium containing 300 mM urea for 2 hours. After washing the cells three times with PBS, cellular organelles were stained with ER tracker, GA tracker, and Lyso tracker, respectively. Confocal laser scanning microscopy (CLSM) was used to observe the fluorescence, and ImageJ software was employed for subsequent analysis.

Penetration Efficiency in Multicellular Spheroids

T24 or 5637 cells were suspended in DMEM containing 0.12% (w/v) methylcellulose at a density of 1×10^6 cells/mL. 25ul of the cell suspension was placed on the lid of a cell culture dish, and 10 mL of PBS was added to the dish to keep the droplet moist. After 72 hours, the formed spheroids were transferred to a low - adhesion 96 - well plate at one spheroid per well and cultured for an additional 72 hours. M@Gem and UG-M@Gem were incubated with Dil (10 μM) for 30 minutes, followed by centrifugation at 12,000 rpm to remove free Dil. UG were incubated with sulfo-NHS-Cy5 (10uM) for 1 hour, followed by centrifugation at 12,000 rpm to remove free sulfo-NHS-Cy5. Fluorescently labeled UG-M@Gem was incubated with the T24 or 5637 spheroids in a medium containing 300 mM urea for 2 hours. After washing twice with PBS, the T24 or 5637 spheroids were imaged using CLSM, and the images were analyzed using ImageJ software.

In vitro Cytotoxicity Assay

T24 and 5637 cells were seeded in 96-well plates at 8,000 cells per well and incubated for 12 hours. The cells were then treated with various concentrations of manganese ions, cell membrane components, and UG-M@Gem in a medium containing 300 mM urea for 24 hours. Cell viability was assessed using the CCK-8 assay.

Transwell and Wound-Healing Assay

T24 and 5637 cells were incubated with the indicated treatments in a medium containing 300 mM urea for 2 hours, and then T24 and 5637 cells were subjected to the indicated treatments and then evaluated for their migration abilities using Transwell assays and wound - healing assays. In Transwell assays, 5×10^5 cells were placed in upper chambers (8.0 μm pore, polyester membrane) with complete medium in the lower chambers. After 24 h, non-migrated cells were removed; migrated cells were fixed with 4% paraformaldehyde, stained with 0.1% crystal violet, and counted via inverted microscopy. For wound - healing assays, cells were cultured to confluence in 6 - well plates (8×10^5 per well). A sterile pipette tip created a wound, followed by treatments in a medium containing 300 mM urea for 2 hours. Wound closure was measured at 24 and 48 h using phase - contrast microscopy.

Therapeutic Effect in vivo

All animal experiments were approved by the Laboratory Animal Management Committee at Zhejiang Provincial People's Hospital (approval no. 20240605085754648534) and raised in a suitable environment in the Experimental Animal Center of Zhejiang Provincial People's Hospital. Female nu/nu mice (6–8 weeks old) were anesthetized with 1% isoflurane and kept on a heated platform during catheterization. Bladders were flushed with sterile PBS, followed by instillation of 100 μL of PBS containing 5×10^5 luciferase-transfected T24 cells for 1 h to establish orthotopic bladder tumors. Lubricated angiocatheters were inserted into the urethra. After full insertion, the bladder was flushed with 80 μL of sterile PBS. The mice were randomly divided into 5 groups (n = 5/group), including (1) PBS, (2) Gem, (3) M@Gem, (4) UG, and (5) UG-M@Gem. All groups received 300 mM urea in conjunction with their respective treatments. In the study, Gem was applied at a dose of 10 mg/kg and retained for 2 hours after intravesical instillation. Mice underwent intravesical instillation every 7 days for a total of 5 sessions, with body weight measurements taken every 5 days. To monitor tumor bioluminescence in vivo, mice received intraperitoneal injections of 100 mg/kg D - luciferin and were imaged using the IVIS Lumina XRMS Series III system (PerkinElmer, Waltham, MA, USA) at 7 - day intervals. One day after the final intravesical instillation, mice were sacrificed, and tissues (bladder, heart, liver, spleen, lung, and kidney) were collected for histopathological analysis via HE staining. Tissue imaging was performed using an inverted microscope (TS 100; Nikon Ti, Japan).

Statistical Analysis

Statistical analysis was performed using Student's *t*-test or one-way ANOVA where applicable. Data are presented as mean ± SD. A two-tailed p-value less than 0.05 was deemed to indicate statistical significance. The levels of significance were denoted as *$p < 0.05$, **$p < 0.01$, ***$p < 0.001$, and ****$p < 0.0001$. All analyses were conducted using GraphPad Prism Version 8.0 (GraphPad Software, San Diego, CA, USA).

Results and Discussion

Characterization of UG-M@Gem

As depicted in Figure 1, our team utilized a straightforward one-step biomimetic mineralization approach to develop UG with three enzyme activities, aiming to overcome the limitations of Gox and urease, such as poor stability, short in vivo half-life, and systemic toxicity.[21] To create an asymmetric structure for rapid nanoparticle motion, we modified the surface of UG with DBCO and coupled it to drug - loaded membrane nanoparticles functionalized with azide groups. The SEM images reveal that the synthesized UG-M@Gem exhibits a uniform dumbbell-shaped structure (Figure 2A). The individual M@Gem and UG have diameters of 120.6±2.9 nm and 206±3.5 nm, respectively, and the coupled dumbbell structure has a diameter of 310±5.1 nm (Figure 2B and S2). Further validation of the composition of the dumbbell structure was conducted through energy-dispersive X-ray spectroscopy (EDS), which showed that Mn, Ni, and S elements are predominantly located in the tail-end UG structure (Figure S3), consistent with the presence of S in Gox and Ni in urease. Additionally, X-ray photoelectron spectroscopy (XPS) survey spectra of UG-M@Gem corroborated these findings (Figure S4). The Fourier-transform infrared spectroscopy (FTIR) of UG-M@Gem show significant differences compared to those of M@Gem and UG, providing direct evidence of successful synthesis (Figure S5). A new characteristic absorption peak for the Mn-O bond appears at 536 cm^{-1}, confirming the biomineralization reaction of Mn^{2+} with Gox and urease. Additionally, the amide I band shifts from 1640 cm^{-1} in M@Gem and 1632 cm^{-1} in UG to 1625 cm^{-1} in UG-M@Gem, while the amide II band shifts from 1547 and 1529 cm^{-1} to 1536 cm^{-1}. These shifts in amide bond peaks clearly indicate interactions between proteins and the formation of a new structure, thus fully demonstrating the successful combination of M@Gem with UG. Zeta-potential measurements indicated that UG-M@Gem possessed a more negative surface charge than either M@Gem or UG alone, which confirms the successful conjugation of the membrane nanoparticles with UG (Figure 2C). Additionally, the enzyme activities of urease and Gox in the three-enzyme nanomotors structure remained comparable to those of the un - polymerized enzymes (Figure 2D). The biomineralization process effectively retains the activity of both GOx and urease. Moreover, the biomineralization synthesis method can significantly maintain the activity of urease (Figure S1). The complex urinary environment, which is typically hypotonic and acidic, poses a challenge to nanoparticle stability.[22] In PBS (pH 7.4), the average size of UG-M@Gem remained stable However, after incubation in artificial urine, the average size of UG-M@Gem decreased, likely due to the acidic environment of urine causing the three-enzyme nanomotors structure to break down (Figure 2E). Recent studies have demonstrated that the movement of synthetic motors can be driven by biocatalytic reactions.[23–25] Urease-powered nanomotors generate CO_2 and NH_3 from urea, enabling self-propulsion. For in vivo applications, urine offers a sustainable urea supply (up to 300 mM),[26] effectively fueling nanomotor motion. The motion of different nanomotors was tracked in simulated urine with low urea concentrations (0, 100, 300 mM) and high urea concentration (500 mM). Over 15 seconds, the mean squared displacement (MSD) of UG-M@Gem increased linearly in low urea concentrations (Figure 2F), indicating brownian motion. In 300 mM urea, the MSD curve rose nonlinearly (Figure 2G), showing directional movement due to self - propulsion. In PBS, UG-M@Gem released 17.6 ± 0.4% of Gem, compared to 35.5 ± 1.6% in urine. Gox, a flavin-dependent enzyme, is prone to inactivation by biotic factors before reaching tumor cells.[21] We assessed the nano platform's ability to stabilize Gox by measuring H_2O_2 levels and pH in glucose solutions at various concentrations. UG-M@Gem treatment caused a sharp increase in H_2O_2 and a pH drop similar to free Gox (Figure 2I and J), proving efficient glucose consumption.

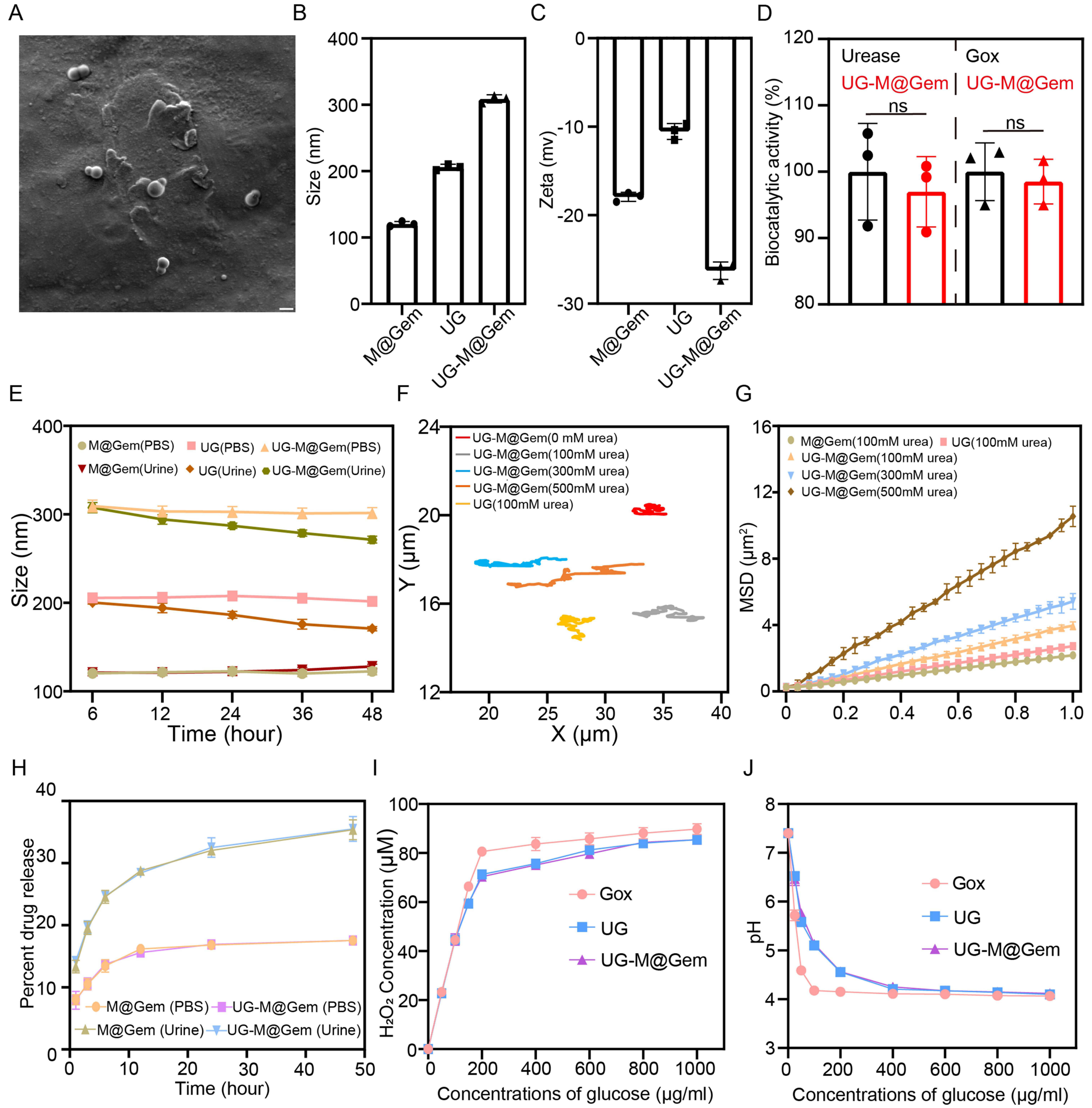

Figure 2 Physicochemical properties of nanomotors. (**A**) SEM image of UG-M@Gem. Scar bar: 100 nm. (**B**) The average size of M@Gem, UG and UG-M@Gem. (**C**) The average zeta potential of M@Gem, UG and UG-M@Gem. (**D**) Urease activity (left) and Gox (right) activity of UG-M@Gem. (**E**) The stability of the size of M@Gem, UG and UG-M@Gem. (**F**) The trajectories of UG-M@Gem (urease: 200U/mL) in simulated urine of different urea concentrations in 15s. (**G**) The mean-square displacement (MSD) analysis of UG-M@Gem in simulated urine of different urea concentrations. (**H**) Drug release profiles of Gem (Gem-eq dose: 20 μg/mL) from M@Gem and UG-M@Gem. (**I**) The concentration of generated H_2O_2 and (**J**) pH values at different time points due to the UG-M@Gem oxidation of glucose (1000 μg/mL). ns indicate $P > 0.05$.

The Transmucosal Transport, Targeting Efficiency and Internalization Behavior of Nanomotors

Subsequently, we examined the penetration efficacy of distinct nanomotor formulations through the urothelial barrier. Given that mucus acts as the initial barrier to intravesical drug delivery, it was central to our evaluation.[21] To this end, we established an artificial mucus layer, approximately 2 mm thick, in the upper Transwell chamber by introducing bladder mucus. Nanoparticles suspended in urea solutions of different concentrations were then applied on top of this layer. In low-urea

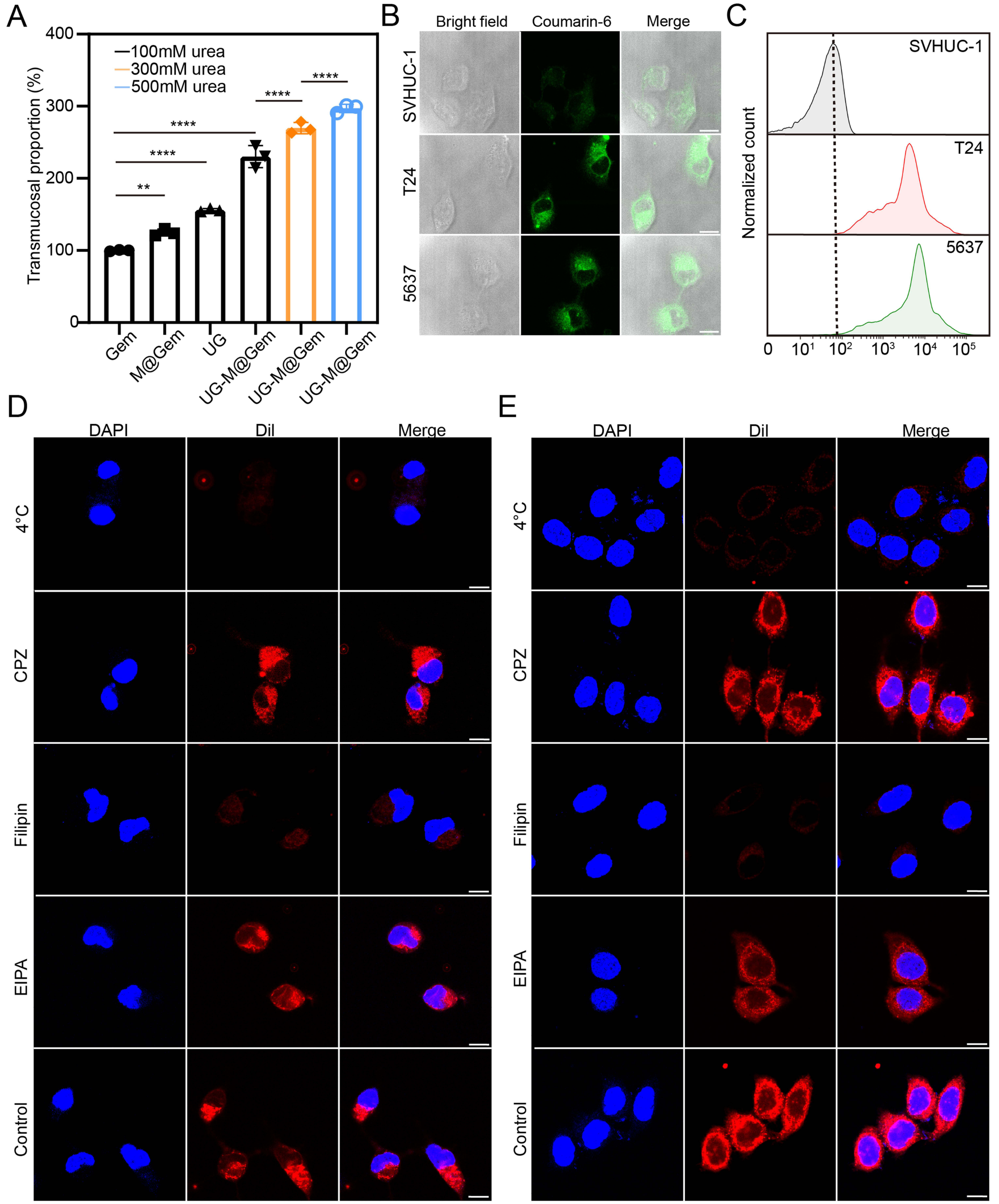

Figure 3 The penetration efficiency, targeting property and endocytosis pathway of nanommotors. (**A**) The Transwell assay was used to evaluate the nanomotors efficiency. (**B**) CLSM analysis of the BCa targeting efficiency of UG-M@Gem. scale bar: 20 μm. (**C**) Flow cytometry analysis of the BCa targeting efficiency of UG-M@Gem. (**D**) CLSM analysis of the endocytosis inhibition by different treatments in T24 and in (**E**) 5637. Scar bar: 25 μm. ** $p < 0.01$, **** $p < 0.0001$.

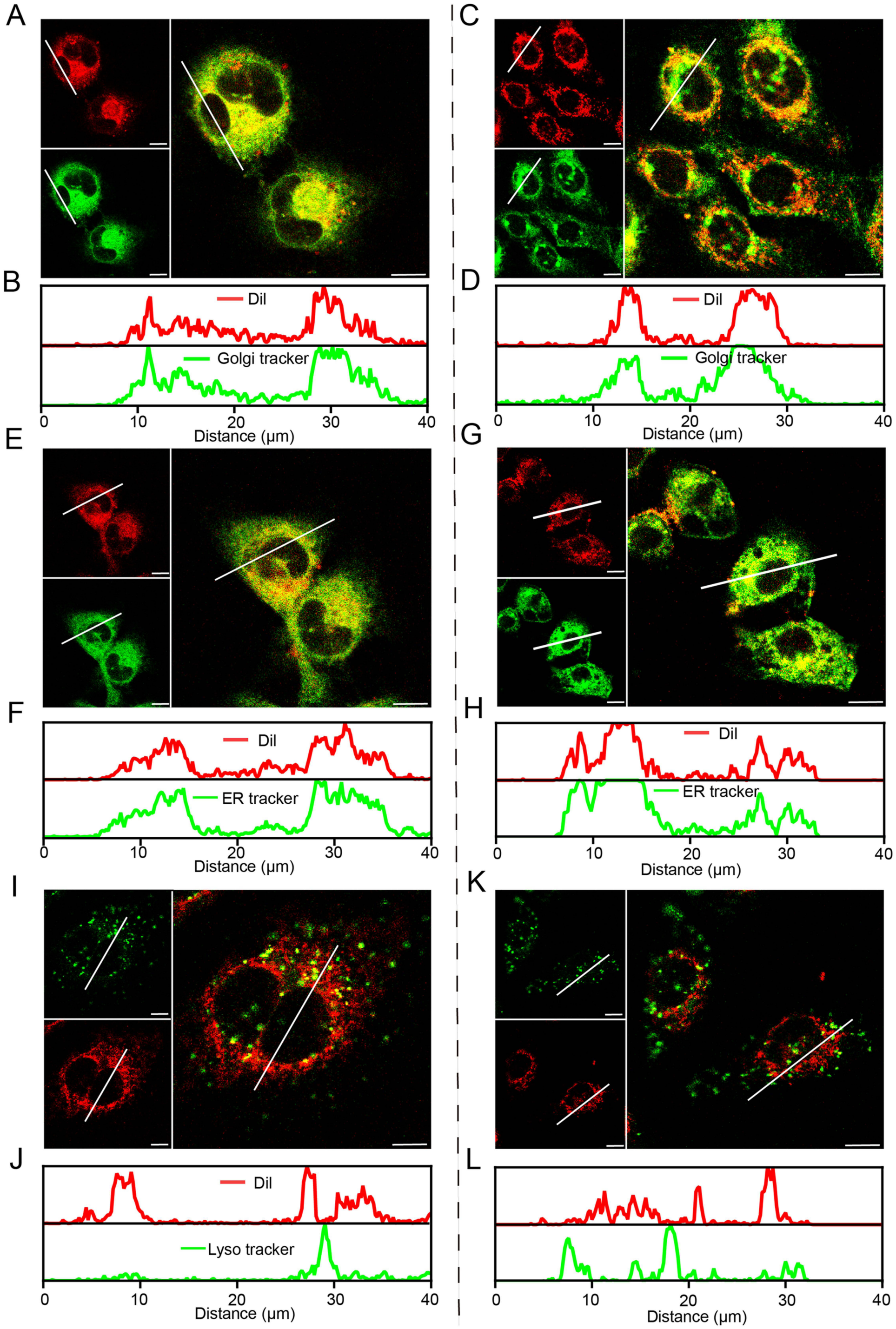

Figure 4 Tumor cell intracellular trafficking of nanomotors (**A**) The subcellular colocalization of UG-M@Gem and Golgi apparatus in T24. (**B**) The statistics of subcellular co-localization of UG-M@Gem and Golgi apparatus in T24. The fluorescence intensity along the white line drawn in (**A**). Red: UG-M@Gem; Green: Golgi tracker; Scar bar: 20 µm. (**C**) The subcellular colocalization of UG-M@Gem and Golgi apparatus in 5637. (**D**) The statistics of subcellular co-localization of UG-M@Gem and Golgi apparatus in 5637. The fluorescence intensity along the white line drawn in (**C**). Red: UG-M@Gem; Green: Golgi tracker; Scar bar: 20 µm. (**E**) The subcellular colocalization of UG-M@Gem and ER in T24. (**F**) The statistics of subcellular co-localization of UG-M@Gem and ER in T24. The fluorescence intensity along the white line drawn in (**E**). Red: UG-M@Gem; Green: ER tracker; Scar bar: 20 µm. (**G**) The subcellular colocalization of UG-M@Gem and ER in 5637. (**H**) The statistics of subcellular co-localization of UG-M@Gem and ER in 5637. The fluorescence intensity along the white line drawn in (**G**). Red: UG-M@Gem; Green: ER tracker; Scar bar: 20 µm. (**I**) The subcellular colocalization of UG-M@Gem and Lysosomes in T24. (**J**) The statistics of subcellular co-localization of UG-M@Gem and Lysosomes in T24. The fluorescence intensity along the white line drawn in (**I**). Red: UG-M@Gem; Green: Lyso tracker; Scar bar: 20 µm. (**K**) The subcellular colocalization of UG-M@Gem and Lysosomes in 5637. (**L**) statistics of subcellular co-localization of UG-M@Gem and Lysosomes in 5637. The fluorescence intensity along the white line drawn in (**K**). Red: UG-M@Gem; Green: Lyso tracker; Scar bar: 20 µm.

conditions, UG-M@Gem demonstrated a significantly higher mucus-penetration efficiency compared to Gem, M@Gem, and UG (Figures 3A and S6). As urea concentration increased, the transmucosal diffusion of UG-M@Gem accelerated. Notably, at a urea concentration of 500 mM, the nanoparticles in UG-M@Gem traversed the artificial mucus layer at the fastest rate, attributed to the robust gas propulsion generated by urease-catalyzed urea decomposition in high-urea environments. However, the transmucosal diffusion efficiency of M@Gem did not improve with increasing urea concentration, likely due to the Brownian motion of these nanoparticles at these concentrations. Additionally, UG demonstrated varying transmucosal efficiencies at different urea concentrations, with higher urea concentrations enhancing UG penetration, though its efficiency remained lower than that of UG-M@Gem. This may be due to the reaction between urease in UG and urea, which promotes UG movement. The targeting efficiency of UG-M@Gem is illustrated in Figures 3B, S7, and S8. The fluorescence intensities of T24 and 5637 cells were 4.6 ± 0.6 and 3.9 ± 0.4 times higher, respectively, than those of the normal urothelial cell line SVHUC-1. Flow cytometry analysis further confirmed the targeting capability of UG-M@Gem (Figure 3C). The high targeting efficiency of UG-M@Gem is attributed to the homologous targeting of the tumor membrane. The endocytosis mechanism was further investigated. CPZ, filipin, and EIPA were used to block clathrin-mediated, caveolin-mediated, and macropinocytic pathways, respectively.[27,28] Incubation at 4 °C inhibited energy-dependent endocytosis.[29] In T24 and 5637 cells, UG-M@Gem endocytosis was significantly blocked by 4 °C or filipin (Figures 3D and S9). These results indicate that the cellular uptake of UG-M@Gem occurs via an energy-dependent endocytic pathway, primarily through caveolae-mediated

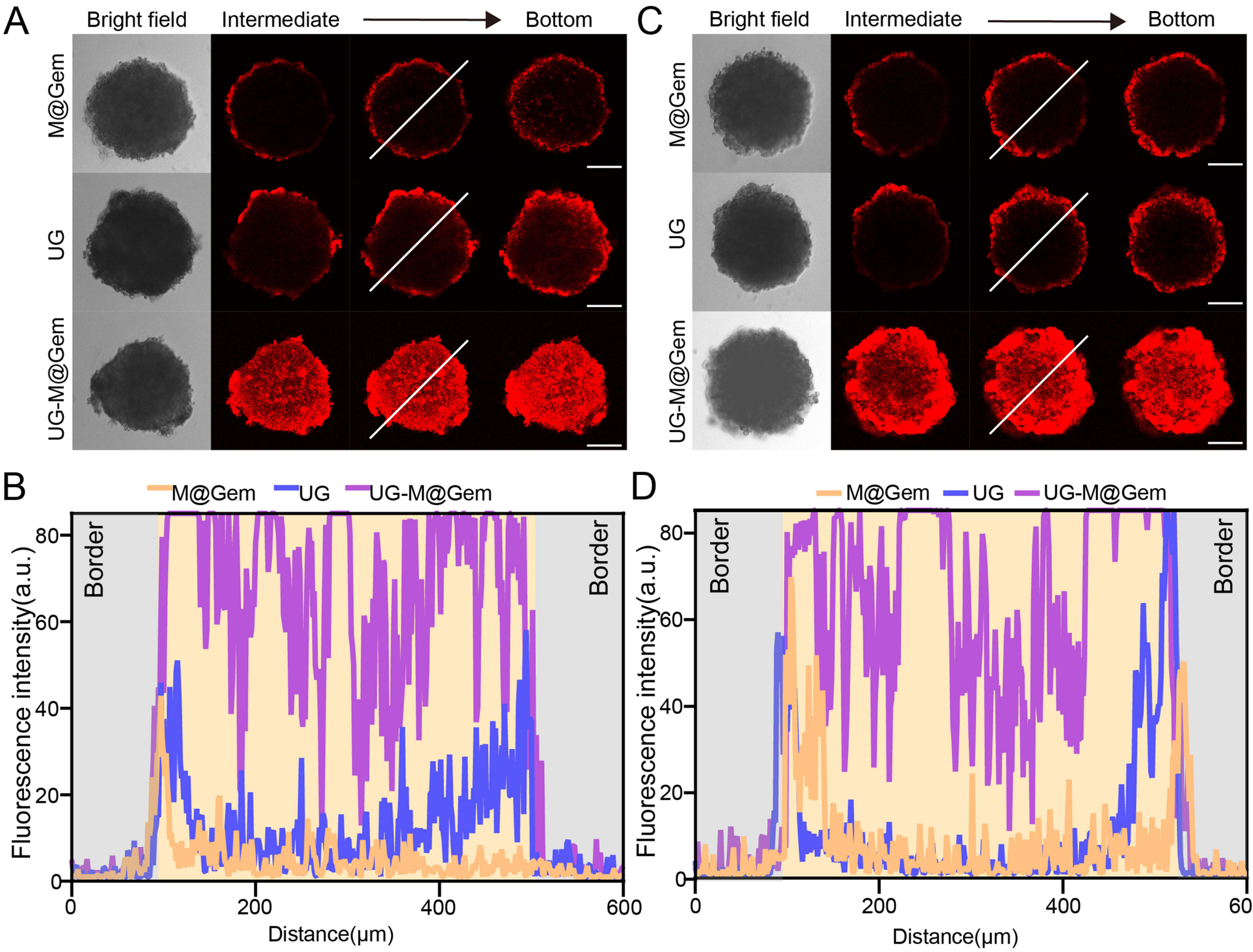

Figure 5 Penetration efficiency in tumor spheroids. (**A**) CLSM analysis of the penetration efficiency of different treatments in T24 tumor spheroids; The Z-stack covered the plane near or along the intermediate layer at 50 μm intervals; Scar bar: 200 μm. (**B**) Dil fluorescence distribution within tumor spheroids from different treatment groups; Fluorescence intensity along the white line in (**A**) was quantified. (**C**) CLSM analysis of the penetration efficiency of different treatments in 5637 tumor spheroids; The Z-stack covered the plane near or along the intermediate layer at 50 μm intervals; Scar bar: 200 μm. (**D**) Dil fluorescence distribution within tumor spheroids from different treatment groups; Fluorescence intensity along the white line in (**C**) was quantified.

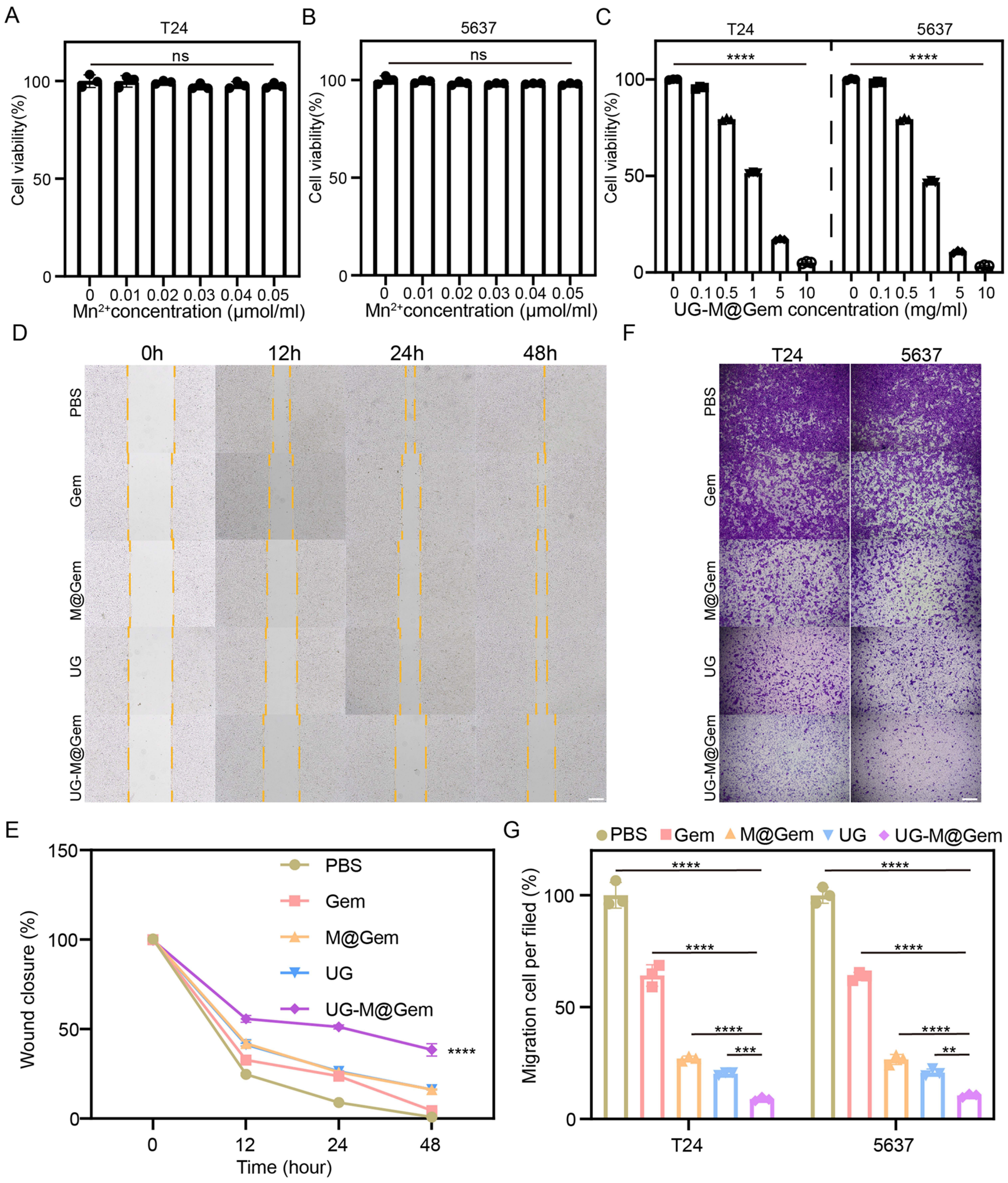

Figure 6 In vitro anticancer activity. (**A**) Cytotoxicity of different concentration of Mn^{2+} for 24 h incubation in T24 and (**B**) 5637. (**C**) Cytotoxicity of different concentration of UG-M@Gem for 24 h incubation. (**D**) The effect and (**E**) statistics of different treatments on T24 cell migration assessed by scratch wound - healing assay. The cell migration boundary was delineated using yellow dotted lines. (**F**) The effects and (**G**) statistics of various treatments on T24 migration evaluated by Transwell assay. scale bar: 200 μm. ** $p < 0.01$, *** $p < 0.001$, **** $p < 0.0001$, ns indicate $P > 0.05$.

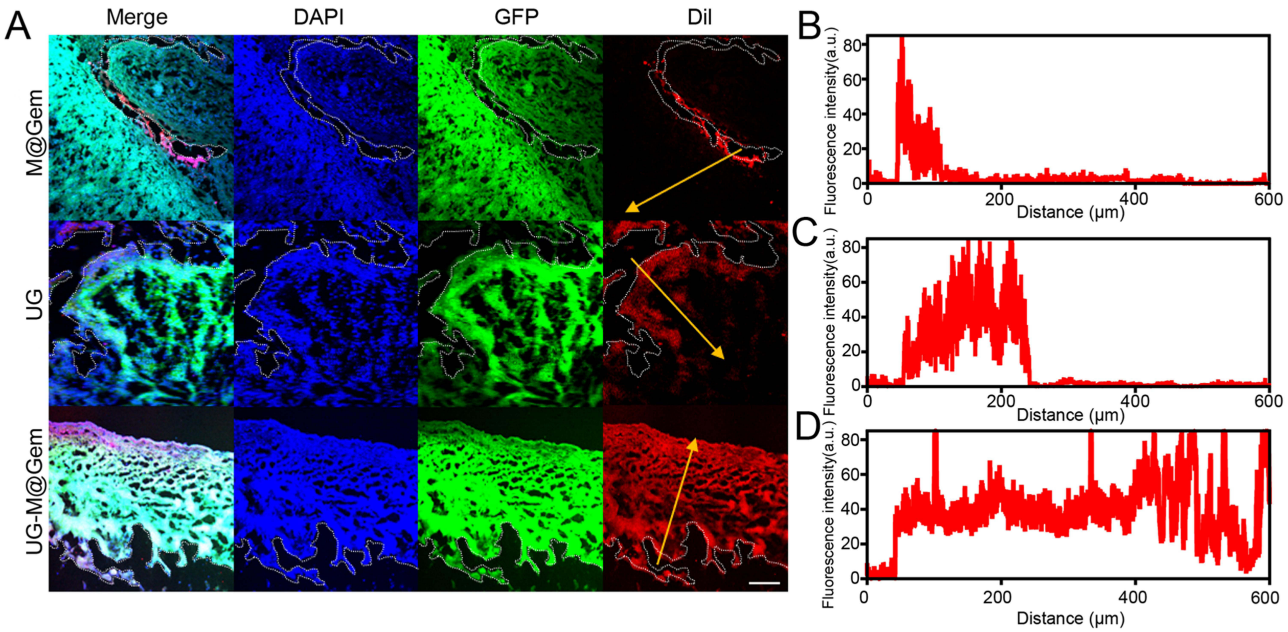

Figure 7 Targetting and penetration of intravesically instilled nanoparticles into the urothelium. (**A**) Distribution of nanoparticles in the urothelium, visualized by Dil fluorescence (red). Nuclei were counterstained with DAPI (blue), and GFP-labeled tumor regions are shown in green. Scale bar: 100 μm. Areas enclosed by white dotted curves indicate the bladder lumen following 2 h of coincubation. The yellow colored arrows indicate from the bladder lumen to the urothelium. (**B-D**) Nanoparticle distribution along the yellow axis in (**A**) from the bladder lumen to the urothelium.

endocytosis. UG-M@Gem was mainly localized to the endoplasmic reticulum and Golgi apparatus, not lysosomes, in T24 and 5637 cells (Figures 4A–L). Thus, the drug payload and UG-M@Gem itself can escape lysosomal degradation.[30]

Penetration Efficiency in Multicellular Spheroids

Multicellular spheroids (MCSs) have been established as in vitro 3D tumor models for evaluating drug penetration into tumors.[31] In this study, we generated T24 and 5637 MCSs to investigate the penetration efficiency of nanomotors. The nanoparticles were surface-labeled with Dil for visualization. As shown in Figure 5A–D, in the M@Gem and UG groups, nanoparticle infiltration was confined to the outer regions of the T24 and 5637 MCSs. In contrast, in the UG-M@Gem group, nanoparticles were able to penetrate into the inner regions of the T24 and 5637 MCSs. These results suggest that the UG-M@Gem nanomotors possess superior penetration capabilities compared to the individual components.

Antitumor Effect in vitro

Before investigating the effects of UG-M@Gem on the proliferation of T24 and 5637 cells, we conducted experiments to exclude potential influences from manganese ions and the cell membrane. As shown in Figures 6A, 6B, S10 and S11, neither manganese ions nor the cell membrane had any significant impact on cell proliferation. Our results demonstrated that UG-M@Gem significantly inhibited the proliferation of T24 and 5637 cells, exhibiting concentration-dependent cytotoxicity (Figure 6C). We determined the concentration of Gem in UG-M@Gem at 10 mg/mL, which was found to be 16.78 μg/mL. Based on this, we selected 20 μg/mL as the highest concentration of free Gem for in vitro antitumor studies. In parallel, we evaluated the in vitro antitumor efficacy of M@Gem at a corresponding Gem concentration of 20 μg/mL. For comparison, UG was also tested at the same concentration as UG-M@Gem in these experiments (Figure S11). Our results show that, at equivalent Gem concentrations, free Gem exhibited significantly weaker cytotoxicity than M@Gem. This difference can be attributed to the enhanced tumor targeting capability of M@Gem, which facilitates its entry into tumor cells in greater quantities via the homologous targeting ability of the tumor cell membrane. Furthermore, UG demonstrated lower cytotoxicity than UG-M@Gem at the same concentration. This suggests that the tumor-targeting properties of the membrane nanomaterials incorporated in UG-M@Gem promote its directional delivery to tumor cells,

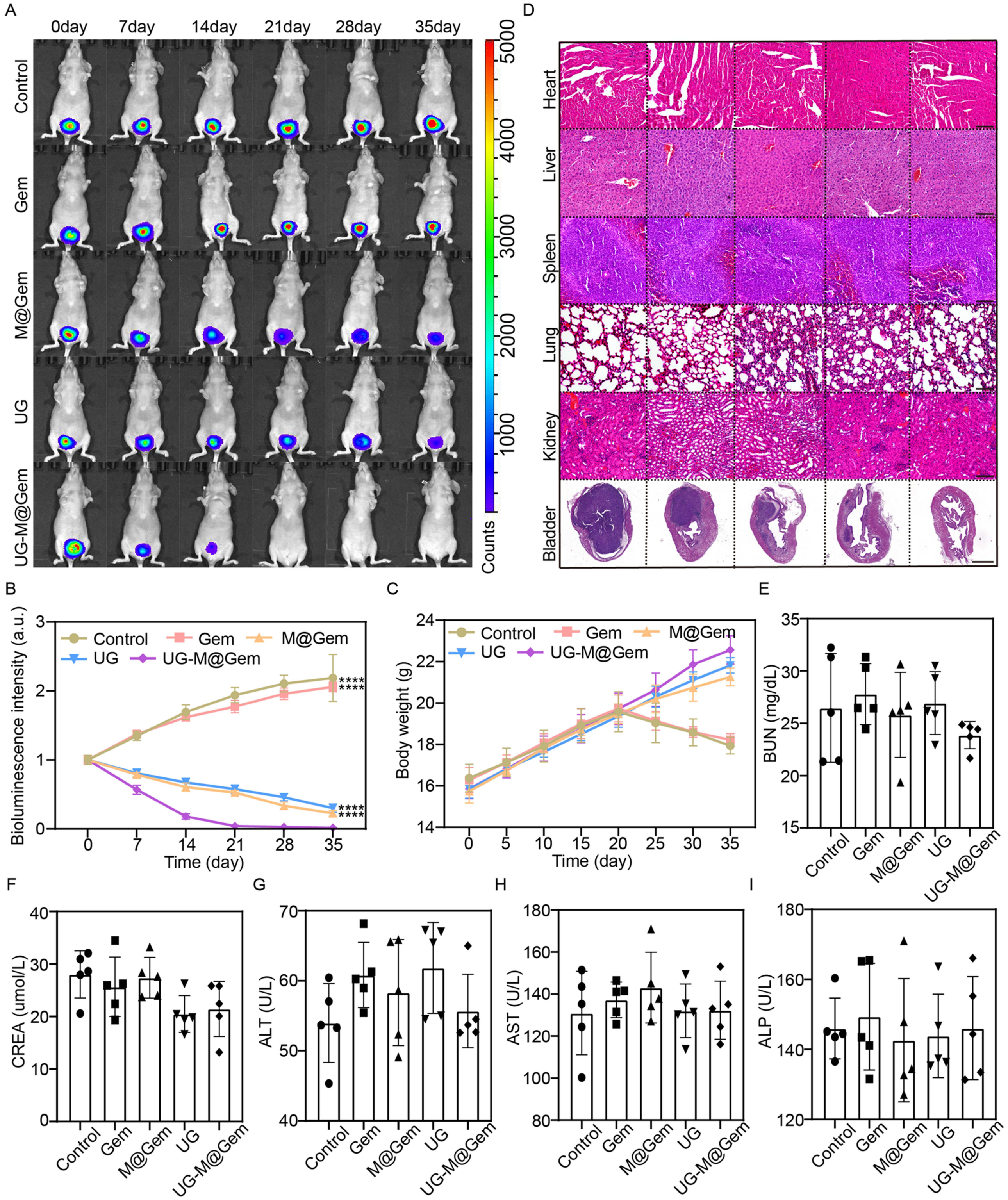

Figure 8 In vivo tumor treatment research of UG-M@Gem. (**A**) In vivo bioluminescence analysis of the anti - tumor activity of different formulations against orthotopic T24 - Luci BCa. (**B**) Changes in the average bioluminescence intensity of orthotopic BCa during intravesical treatment in different groups. (**C**) Changes in the average body weight of murine during intravesical treatment in different groups. (**D**) H&E staining results of normal organs and bladders after treatment from different groups of murine. (**E–I**) Biochemical profiling of blood samples from different groups. **** $p < 0.0001$.

enhancing its therapeutic efficacy. Moreover, UG-M@Gem displayed the most pronounced inhibitory effect on cell migration, as evidenced by scratch wound - healing and Transwell migration assays (Figures 6D–G).

The Targeting and Permeability of Nanomotors in vivo

The murine orthotopic BCa model is considered the optimal choice for evaluating the in vivo targeting and penetration efficiency of intravesically administered drugs.[32–35] However, within the limited instillation time, most drugs exhibit targeting and penetration levels that fall well below expectations.[36] As shown in Figure 7A–D, UG-M@Gem demonstrated specific accumulation in the tumor region and effectively penetrated the tumor tissue throughout the bladder. The penetration of both UG and M@Gem was limited to the lumen surface or superficial layers of the bladder tissue, which is consistent with the results observed in multicellular spheroid assays. The specific accumulation of UG-M@Gem in tumor regions, as well as its enhanced tumor penetration ability, can be attributed to the directional movement and tumor-targeting properties of UG-M@Gem.

Therapeutic Effects of Nanomotors in vivo

The in vivo antitumor efficacy of the nanomotors was further evaluated in a murine orthotopic BCa model. Free Gem showed rapid tumor growth with minimal inhibition, only slightly less than the control group, which may be attributed to its low tumor targeting and penetration. In contrast, M@Gem and UG partially suppressed tumor growth, thanks to the homing ability of drug-loaded tumor-membrane nanoparticles and increased endocytosis from UG's rapid urinary motion, alongside intracellular glucose depletion by Gox and manganese ions.UG-M@Gem not only achieved the most significant tumor suppression but also completely eliminated tumors by the study's end, with no recurrence within 35 days of follow-up, showing a 100% tumor inhibition rate, surpassing M@Gem (77.3%) and UG (69.8%) (Figure 8A and B). Mice in tumor-suppressed groups showed stable weight gains, while those in disease progression groups had significant weight loss after mid-treatment (Figure 8C). Histopathological H&E staining of major organs revealed no significant changes across treatment groups (Figure 8D). Notably, no residual BCa was detected in UG-M@Gem-treated mice, whereas other groups had invasive tumors affecting the muscularis. No signs of hepatic or renal dysfunction were observed in any group (Figure 8E–I). Overall, these results demonstrate the superior therapeutic efficacy and safety of UG-M@Gem for intravesical BCa treatment.

Conclusion

In summary, we developed a novel dual - spherical nanomotor - based drug - delivery platform for intravesical BCa therapy. This platform integrates tumor - membrane nanoparticles with tri - enzyme - loaded nanoparticles constructed via biomineralization. Our findings demonstrate that these nanomotors exhibit rapid self - propelled motion in urine, enabling effective penetration of the bladder mucosal barrier and deep tumor - targeted delivery. Notably, intravesical instillation of these nanomotors achieved a chemical tumor - resection - like effect in most cases. These preclinical data provide compelling evidence supporting the potential of these dual - spherical nanomotors as a promising platform for BCa treatment and warrant further exploration for clinical translation.

Data Sharing Statement

No datasets were generated or analysed during the current study.

Acknowledgments

The authors are thankful to the National Natural Science Foundation of China (82300868, 82473503) for funding this work.

Disclosure

The authors report no conflicts of interest in this work.

References

1. Malta M. LGBTQ+ health: tackling potential health-care professionals' bias. *Nat Rev Dis Primers*. 2023;9(11):1. doi:10.1038/s41572-022-00413-2
2. Lopez-Beltran A, Cimadamore A, Blanca A, et al. Immune checkpoint inhibitors for the treatment of bladder cancer. *Cancers*. 2021;13(1):131. doi:10.3390/cancers13010131
3. Babjuk M, Burger M, Capoun O, et al. European association of urology guidelines on non-muscle-invasive bladder cancer (Ta, T1, and Carcinoma in Situ). *European Urology*. 2022;81(1):75–94. doi:10.1016/j.eururo.2021.08.010
4. Jiao B, Liu K, Gong H, et al. Bladder cancer selective chemotherapy with potent NQO1 substrate Co-Loaded prodrug nanoparticles. *J Controlled Release*. 2022;347:632–648. doi:10.1016/j.jconrel.2022.05.031
5. Dunsmore J, Duncan E, Mariappan P, et al. What influences adherence to guidance for postoperative instillation of intravesical chemotherapy to patients with bladder cancer? *BJU International*. 2021;128(2):225–235. doi:10.1111/bju.15336
6. Sung H, Ferlay J, Siegel RL, et al. Global cancer statistics 2020: GLOBOCAN estimates of incidence and mortality worldwide for 36 cancers in 185 countries. *CA A Cancer J Clin*. 2021;71(3):209–249. doi:10.3322/caac.21660
7. Paxton WF, Kistler KC, Olmeda CC, et al. Catalytic nanomotors: autonomous movement of striped nanorods. *J Am Chem Soc*. 2004;126 (41):13424–13431. doi:10.1021/ja047697z
8. Fournier-Bidoz S, Arsenault AC, Manners I, Ozin GA. Synthetic self-propelled nanorotors. *Chem Commun*. 2005;4:441–443. doi:10.1039/b414896g
9. Katuri J, Ma X, Stanton MM, Sánchez S. Designing micro- and nanoswimmers for specific applications. *Acc Chem Res*. 2017;50(1):2–11. doi:10.1021/acs.accounts.6b00386
10. Sánchez S, Soler L, Katuri J. Chemically powered micro- and nanomotors. *Angewandte Chemie*. 2015;54(5):1414–1444. doi:10.1002/anie.201406096
11. Schamel D, Mark AG, Gibbs JG, et al. Nanopropellers and their actuation in complex viscoelastic media. *ACS Nano*. 2014;8(9):8794–8801. doi:10.1021/nn502360t
12. Peng F, Tu Y, Men Y, van Hest JC, Wilson DA. Supramolecular adaptive nanomotors with magnetotaxis behavior. *Advanc Material*. 2017;29(6). doi:10.1002/adma.201604996
13. Fu LH, Qi C, Hu YR, Lin J, Huang P. Glucose oxidase-instructed multimodal synergistic cancer therapy. advanced materials (Deerfield beach. *Fla.)*. 2019;31(21):e1808325. doi:10.1002/adma.201808325
14. Yang B, Shi J. Chemistry of advanced nanomedicines in cancer cell metabolism regulation. *Advanc Sci*. 2020;7(18):2001388. doi:10.1002/advs.202001388
15. Zhang T, Zhang Z, Yue Y, et al. A general hypoxia-responsive molecular container for tumor-targeted therapy. *Advanc Materials*. 2020;32(28): e1908435. doi:10.1002/adma.201908435
16. Zhang C, Hu J, Jiang Y, et al. Biomineralization-inspired synthesis of amorphous manganese phosphates for GLUT5-targeted drug-free catalytic therapy of osteosarcoma. *Nanoscale*. 2022;14(3):898–909. doi:10.1039/d1nr06220d
17. Cao Z, Zhang L, Liu J, et al. A dual enzyme-mimicking radical generator for enhanced photodynamic therapy via series-parallel catalysis. *Nanoscale*. 2021;13(41):17386–17395. doi:10.1039/d1nr04104e
18. Korupalli C, Kuo -C-C, Getachew G, et al. Multifunctional manganese oxide-based nanocomposite theranostic agent with glucose/light-responsive singlet oxygen generation and dual-modal imaging for cancer treatment. *J Colloid Interface Sci*. 2023;643:373–384. doi:10.1016/j.jcis.2023.04.049
19. Yang X, Yang Y, Gao F, Wei -J-J, Qian C-G, Sun M-J. Biomimetic hybrid nanozymes with self-supplied h^+ and accelerated o_2 generation for enhanced starvation and photodynamic therapy against hypoxic tumors. *Nano Lett*. 2019;19(7):4334–4342. doi:10.1021/acs.nanolett.9b00934
20. Mou Y, Liu Z, Xu W, et al. Dual-source powered sea urchin-like nanomotors for intravesical photothermal therapy of bladder cancer. *J Nanobiotechnol*. 2025;23(1):355. doi:10.1186/s12951-025-03446-3
21. Fu L-H, Hu Y-R, Qi C, et al. Biodegradable manganese-doped calcium phosphate nanotheranostics for traceable cascade reaction-enhanced anti-tumor therapy. *ACS Nano*. 2019;13(12):13985–13994. doi:10.1021/acsnano.9b05836
22. Hamamoto S, Takemura T, Suzuki K, Nishimura T. Effects of pH on nano-bubble stability and transport in saturated porous media. *J Contaminant Hydrol*. 2018;208:61–67. doi:10.1016/j.jconhyd.2017.12.001
23. Jiang Z, Fu L, Wei C, Fu Q, Pan S. Antibacterial micro/nanomotors: advancing biofilm research to support medical applications. *J Nanobiotechnol*. 2023;21(1):388. doi:10.1186/s12951-023-02162-0
24. Lv Y, Pu R, Tao Y, et al. Applications and future prospects of micro/nanorobots utilizing diverse biological carriers. *Micromachines*. 2023;14 (5):983. doi:10.3390/mi14050983
25. Choi H, Cho SH, Hahn SK. Urease-powered polydopamine nanomotors for intravesical therapy of bladder diseases. *ACS Nano*. 2020;14 (6):6683–6692. doi:10.1021/acsnano.9b09726
26. Liu L, Mo H, Wei S, Raftery D. Quantitative analysis of urea in human urine and serum by^{1}H nuclear magnetic resonance. *Analyst*. 2012;137 (3):595–600. doi:10.1039/c2an15780b
27. Yılmaz D, Culha M. Investigation of the pathway dependent endocytosis of gold nanoparticles by surface-enhanced raman scattering. *Talanta*. 2021;225:122071. doi:10.1016/j.talanta.2020.122071
28. Simian hemorrhagic fever virus cell entry is dependent on CD163 and uses a clathrin-mediated endocytosis-like pathway. Available from. https://pubmed.ncbi.nlm.nih.gov/25355889/. Accessed December 1, 2025.
29. Nagai N, Ogata F, Otake H, Nakazawa Y, Kawasaki N. Energy-dependent endocytosis is responsible for drug transcorneal penetration following the instillation of ophthalmic formulations containing indomethacin nanoparticles. *IJN*. 2019;14:1213–1227. doi:10.2147/IJN.S196681
30. Liu C-G, Han Y-H, Kankala RK, Wang S-B, Chen A-Z. Subcellular performance of nanoparticles in cancer therapy. *IJN*. 2020;15:675–704. doi:10.2147/IJN.S226186
31. Isono M, Okubo K, Asano T, Sato A. Inhibition of checkpoint kinase 1 potentiates anticancer activity of gemcitabine in bladder cancer cells. *Sci Rep*. 2021;11(1):10181. doi:10.1038/s41598-021-89684-5
32. Zhou Q, Shao S, Wang J, et al. Enzyme-activatable polymer–drug conjugate augments tumour penetration and treatment efficacy. *Nat. Nanotechnol*. 2019;14(8):799–809. doi:10.1038/s41565-019-0485-z

33. Huebner D, Rieger C, Bergmann R, et al. An orthotopic xenograft model for high-risk non-muscle invasive bladder cancer in mice: influence of mouse strain, tumor cell count, dwell time and bladder pretreatment. *BMC Cancer*. 2017;17(1):790. doi:10.1186/s12885-017-3778-3
34. Roelants M, Van Cleynenbreugel B, Van Poppel H, Lerut E, de Witte PAM. Use of fluorescein isothiocyanate-human serum albumin for the intravesical photodiagnosis of non-muscle-invasive bladder cancer: an in vitro study using multicellular spheroids composed of normal human urothelial and urothelial cell carcinoma cell lines. *BJU Int*. 2011;108(3):455–459. doi:10.1111/j.1464-410X.2010.09951.x
35. Vasyutin I, Zerihun L, Ivan C, Atala A. Bladder organoids and spheroids: potential tools for normal and diseased tissue modelling. *Anticancer Res*. 2019;39(3):1105–1118. doi:10.21873/anticanres.13219
36. Abidine Y, Giannetti A, Revilloud J, Laurent VM, Verdier C. Viscoelastic properties in cancer: from cells to spheroids. *Cells*. 2021;10(7):1704. doi:10.3390/cells10071704